

1      **Impact of grids and dynamical cores in CESM2.2 on**  
2      **the surface mass balance of the Greenland Ice Sheet**

3      **Adam R. Herrington** <sup>1</sup>, **Marcus Lofverstrom** <sup>2</sup>, **Peter H. Lauritzen** <sup>1</sup> and  
4      **Andrew Gettelman** <sup>1</sup>

5      <sup>1</sup>National Center for Atmospheric Research, 1850 Table Mesa Drive, Boulder, Colorado, USA

6      <sup>2</sup>Department of Geosciences, University of Arizona, 1040 E. 4th Street, Tucson, AZ USA

7      **Key Points:**

- 8      • enter point 1 here  
9      • enter point 2 here  
10     • enter point 3 here

**Abstract**

[ enter your Abstract here ]

**Plain Language Summary**

[ enter your Plain Language Summary here or delete this section]

**1 Introduction**

General Circulation Models (GCMs) are powerful tools for understanding the meteorology and climate of the high-latitudes, which are among the most sensitive regions on Earth to global and environmental change. Despite their importance, the numerical treatment of polar regions in GCMs is handled in vastly-different ways due to the so-called *pole-problem* (D. Williamson, 2007), which refers to numerical instability arising from the convergence of meridians at the polar points on latitude-longitude grids (e.g., Figure 1a). Depending on the numerics, methods exist to suppress this instability, and latitude-longitude grids may be advantageous for polar processes as structures can be represented with more degrees of freedom than elsewhere in the computational domain. With the recent trend towards globally uniform unstructured grids, any potential benefits of latitude-longitude grids on polar regions may become a relic of the past. In this study, a spectrum of model grids and dynamical cores (hereafter referred to as *dycores*) available in the Community Earth System Model, version 2.2 (CESM; <http://www.cesm.ucar.edu/models/cesm2/>) are evaluated to understand their impacts on the simulated characteristics of the Arctic, with a special focus on the meteorology over the Greenland Ice Sheet.

In the 1970's the pole problem was largely defeated through wide-spread adoption of efficient spectral transform methods in GCMs. These methods transform grid point fields into a global, isotropic representation in wave space, where linear operators (e.g. horizontal derivatives) in the equation set can be solved for exactly. While spectral transform methods are still used in the 21st century, local numerical methods have become desirable for their ability to run efficiently on massively parallel systems. The pole-problem has thus re-emerged in contemporary climate models that use latitude-longitude grids, and some combination of reduced grids and polar filters are necessary to ameliorate this instability (Jablonowski & Williamson, 2011). Polar filters are akin to a band-aid; they subdue the growth of unstable modes by applying additional damping to the solution over polar regions. One might expect that this additional damping reduces the effective resolution such that the resolved scales are similar across the entire domain, but this seems unlikely (describe why) and is explored further in this study.

An alternative approach is to use unstructured grids, which allow for more flexible grid structures that permit quasi-uniform grid spacing globally and eliminates the pole-problem entirely (e.g., Figure 1c). This grid flexibility also allows for variable-resolution or regional grid refinement (e.g., Figure 2). Grids can be developed with refinement over polar regions that could in principle make up for any loss in polar resolution in transitioning away from latitude-longitude grids (e.g., Figure 2), although this comes at the cost of a smaller CFL-limiting time-step in the refined region (the CFL-condition — short for Courant–Friedrichs–Lowy condition — is a necessary condition for numerical stability when using discrete data in time and space). However, unstructured grids scale more efficiently on parallel systems than latitude-longitude grids, likely resulting in a greater prevalence of unstructured grids as computing power continued to increase over time.

The meteorology and climate of the Arctic is characterized by a range of processes and scales that are difficult to represent in GCMs (Bromwich et al., 2001; Smirnova & Golubkin, 2017; van Kampenhout et al., 2018). For example, while synoptic scale storms

are generally well represented at typical GCM resolutions of 1 to 2 degrees (Jablonowski & Williamson, 2006; Stocker, 2014), mesoscale Polar Lows are not well resolved at these resolutions. These mesoscale systems are prevalent during the cold season and produce gale-force winds that can induce large heat and moisture fluxes through the underlying sea-ice/ocean interface. The Arctic also contains the Greenland Ice Sheet (hereafter denoted as *GrIS*). While it blankets the largest island in the world (Greenland), many of the processes that control the *GrIS* annual surface mass balance (the integrated sum of precipitation and melting) are only partially resolved at typical GCM resolutions. For example, *GrIS* precipitation is typically confined to the ice-sheet margins (predominately the southeastern margin) where orographic precipitation is generated by steep topographic slopes. Moreover, *GrIS* ablation areas (marginal regions where seasonal melting exceeds the annual mass input from precipitation) are typically 10s to 100 km wide and confined to low-level areas or regions with limited precipitation. GCMs struggle to resolve the magnitude and extent of these features (van Kampenhout et al., 2018), which can lead to unrealistic ice sheet growth in models with an interactive ice sheet component (e.g., Lofverstrom et al., 2020).

The goal of this study is to characterize the representation of high-latitude regions using the spectral-element and finite-volume dycores in CESM2.2, as these models treat the high-latitudes, e.g., the pole-problem, in different ways. The manuscript is laid out as follows: Section 2 consists of documentation of the grids, dycores and physical parameterizations used in this study. The Arctic refined grids were developed by the authors, and this section serves as their official documentation in CESM2.2. Section 2 also contains a description of the experiments along with reanalysis datasets and post-processing software used for evaluating the model simulations. Section 3 contains the results of the experiments, followed by Section 4 that provides a general discussion and conclusions.

## 2 Methods

### 2.1 Dynamical cores

The atmospheric component of CESM2.2, the Community Atmosphere Model, version 6.3 (CAM; <https://ncar.github.io/CAM/doc/build/html/index.html>), supports a number of different atmospheric dynamical cores. These include dycores using latitude-longitude grids, such as finite-volume (FV; Lin, 2004) and eulerian spectral transform (EUL; Collins et al., 2006) models, and dycores built on unstructured grids, including spectral-element (SE; Lauritzen et al., 2018) and finite-volume 3 (FV3; Putman & Lin, 2007) models. The EUL dycore is the oldest dycore in CAM, and the least supported of all the dycores in the current model. FV3 is the newest dycore in CAM, but it was not fully incorporated at the time this work commenced; both the EUL and FV3 dycores are omitted from this study. As such, the results presented in this study are comparing the performance of the SE and FV dycores.

#### 2.1.1 Finite-volume (FV) dynamical core

The FV dycore is a hydrostatic model that integrates the equations of motion using a finite-volume discretization on a spherical latitude-longitude grid (Lin & Rood, 1997). The 2D dynamics evolve in floating Lagrangian layers that are periodically mapped to Eulerian reference grid in the vertical (Lin, 2004), using a hybrid-pressure vertical coordinate. Hyperviscous damping is applied to the divergent modes while Laplacian damping is applied to momentum in the top few layers, referred to as a *sponge layer* (Lauritzen et al., 2011). A polar filter is used to avoid computational instability due to the convergence of the meridians, allowing for a more practical time-step. It takes the form of a Fourier filter in the zonal direction, with the damping coefficients increasing monotonically in the poleward direction (Suarez & Takacs, 1995).

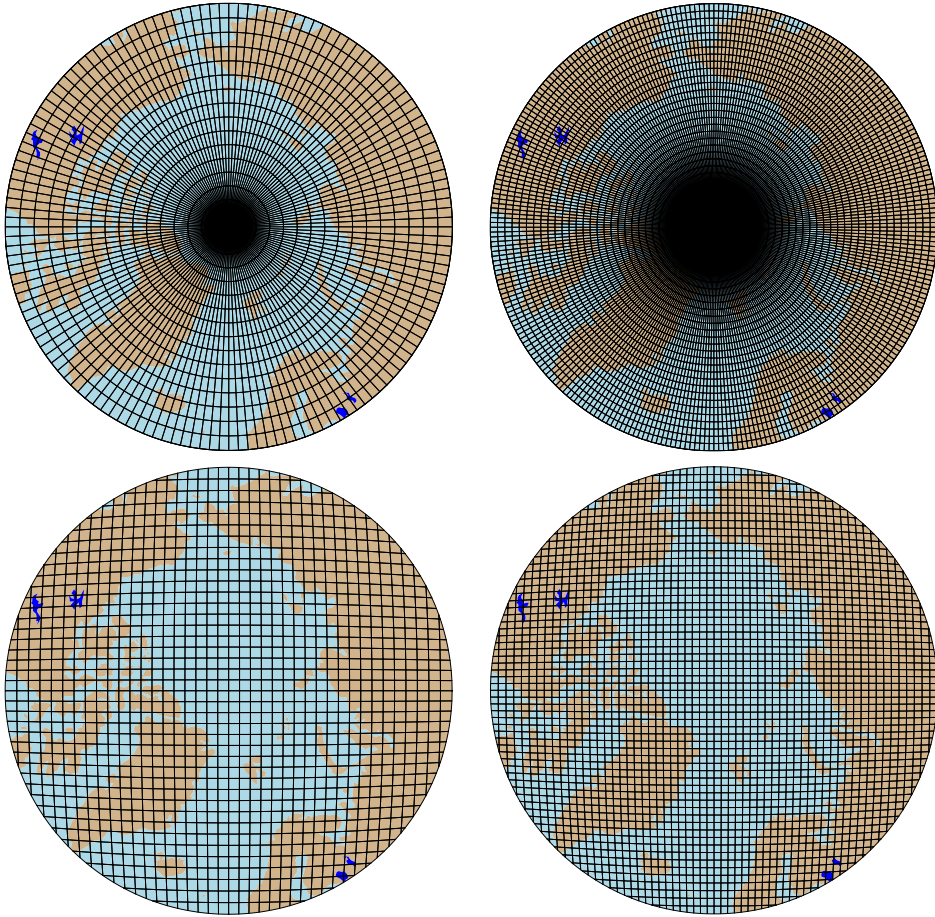


**Figure 1.** Computational grids for the uniform  $1^\circ - 2^\circ$  grids in this study.

### 108            2.1.2 Spectral-element (SE) dynamical core

109            The SE dycore is a hydrostatic model that integrates the equations of motion us-  
 110            ing a high-order continuous Galerkin method (Taylor et al., 1997; Dennis et al., 2012).  
 111            The computational domain is a cubed-sphere grid tiled with quadrilateral elements (e.g.,  
 112            Figure 2). Each element contains a fourth order basis set in each horizontal direction,  
 113            with the solution defined at the roots of the basis functions, the Gauss-Lobatto-Legendre  
 114            (GLL) quadrature points. This results in 16 GLL nodal points within each element, with  
 115            12 of the points lying on the (shared) element boundary. Communication between el-  
 116            ements happens via the direct stiffness summation (Canuto et al., 2007), which applies  
 117            a numerical flux to the element boundaries that reconciles overlapping nodal values and  
 118            produces a continuous global basis set.

119            As with the FV dycore, the dynamics evolve in floating Lagrangian layers that are  
 120            subsequently mapped to an Eulerian reference grid. A dry mass vertical coordinate was  
 121            more recently implemented for thermodynamic consistency with condensates (Lauritzen  
 122            et al., 2018). The 2D dynamics have no implicit dissipation and so hyperviscosity op-  
 123            erators are applied to all prognostic variables to remove spurious numerical errors (Dennis  
 124            et al., 2012). Laplacian damping is applied in the sponge layer.

125            The SE dycore supports regional grid refinement via its variable-resolution config-  
 126            uration, requiring two enhancements over uniform resolution grids. (1) As the numer-



**Figure 2.** Spectral-element grid for the variable-resolution ARCTIC grid in this study. Note that this is not the computational grid; each element has  $3 \times 3$  independent grid points.

ical viscosity increases with resolution, explicit hyperviscosity relaxes according to the local element size, reducing in strength by about an order of magnitude per halving of the grid spacing. A tensor-hyperviscosity formulation is used (Guba et al., 2014), which adjusts the coefficients in two orthogonal directions to more accurately target highly distorted quadrilateral elements. (2) The topography boundary conditions need to be smoothed in a way that does not excite grid scale modes, and so the NCAR topography software (Lauritzen et al., 2015) was modified to scale the smoothing radius by the local element size.

For spectral-element grids with quasi-uniform grid spacing, a variant in which tracer advection is computed using the Conservative Semi-Lagrangian Multi-tracer transport scheme (CSLAM) is used instead (Lauritzen et al., 2017). CSLAM has improved tracer property preservation and accelerated multi-tracer transport. It uses a separate grid from the spectral-element dynamics, through dividing each element into  $3 \times 3$  control volumes with quasi-equal area. The physical parameterizations are computed from the state on the CSLAM grid, which has clear advantages over the default SE dycore in which the physics are evaluated at the GLL nodal points (A. Herrington et al., 2018).

## 2.2 Grids

Six grid are evaluated in this study (Table X). The FV dycore is run with  $1^\circ$  and  $2^\circ$  grid spacing, referred to as *f09* and *f19*, respectively (Figure 1a,b). The  $1^\circ$  equivalent of the CAM-SE-CSLAM grid is also run, referred to as *ne30pg3* (Figure 1c), where *ne* refers to a grid with of  $ne \times ne$  elements per cubed-sphere face, and *pg* denotes that there are  $pg \times pg$  control volumes per element for computing the physics. An additional  $1^\circ$  CAM-SE-CSLAM grid is run, but with the physical parameterizations computed on a grid that contains  $2 \times 2$  control volumes per element, *ne30pg2* (Figure 1d; A. R. Herrington et al., 2019).

Two variable resolution meshes were developed as part of the CESM2.2 release that contains grid refinement over the Arctic (Figure 2). The Arctic meshes were developed using the software package SQuadgen (<https://github.com/ClimateGlobalChange/squadgen>). The *ARCTIC* grid is a  $1^\circ$  grid with  $\frac{1}{4}^\circ$  regional refinement over the broader Arctic region. The *ARCTICGRIS* grid is identical to the *ARCTIC* grid, but contains an additional patch covering the big island of Greenland with  $\frac{1}{8}^\circ$  resolution.

### 158      2.3 Physical parameterizations

159      The CAM6 physical parameterization package (hereafter referred to as the *physics*;  
 160      <https://ncar.github.io/CAM/doc/build/html/index.html>) is used for all simula-  
 161      tions in this study. CAM6 physics is most noteably different from it's predecessors through  
 162      the incorporation of high-order turbulence closure, Cloud Layers Unified by Binormals  
 163      (CLUBB; Golaz et al., 2002; Bogenschutz et al., 2013), which jointly acts as a PBL, shal-  
 164      low convection and cloud macrophysics scheme. CLUBB is coupled with the MG2 mi-  
 165      crophysics scheme (Gettelman et al., 2015), with prognostic precipitation and classical  
 166      nucleation theory in representing cloud ice for improved cloud-aerosol interactions. Deep  
 167      convection is parameterized using a convective quasi-equilibrium mass flux scheme (Zhang  
 168      & McFarlane, 1995; Neale et al., 2008) inclusing convective momentum transport (Richter  
 169      et al., 2010). PBL form drag is modeled after (Beljaars et al., 2004) and orographic grav-  
 170      ity wave drag is represented with an anisotropic method informed by the orientation of  
 171      topographic ridges at the sub-grid scale.

172      The CAM convention is that the physics package determines the vertical resolu-  
 173      tion. Since all runs use CAM6 physics, all grids and dycores use 32 levels in the verti-  
 174      cal, with a model top of about 1 hPa or about 40 km. The physics time-step, in con-  
 175      trast, is dependent on grid resolution. Increases in horizontal resolution permit faster  
 176      vertical velocities that reduce characteristic time-scales, and so the physics time-step should  
 177      be reduced to avoid large time truncation errors (A. Herrington & Reed, 2018). The *ARCTIC*  
 178      and *ARCTICGRIS* grids are therefore run with a 4× and 8× reduction in physics time-  
 179      step relative to the default 1800 s time-step used in coarser, uniform resolution grids.

### 180      2.4 Experimental design

181      All grids and dycores are run using an identical transient 1979-1998 AMIP-style  
 182      configuration, with prescribed monthly SST/sea-ice after (Hurrell et al., 2008). This con-  
 183      figuration refers to the *FHIST compset* and runs out of the box in CESM2.2. The Com-  
 184      munity Land Model (CLM5; [https://escomp.github.io/ctsm-docs/versions/release](https://escomp.github.io/ctsm-docs/versions/release-clm5.0/html/users_guide/index.html)  
 185      -clm5.0/html/users\_guide/index.html), which uses the same grid as the atmosphere  
 186      grid, calculates the surface energy balance at each land tile within a grid cell, which is  
 187      used to compute snow and bare ice melting to inform the surface mass balance (SMB)  
 188      of a glacier unit (van Kampenhout et al., 2020a). For land ice tiles coinciding with the  
 189      Antarctic and Greenland Ice Sheets, the surface energy and mass balance are evaluated  
 190      at ten elevation classes, and integrated over sub-grid hypsometric area-elevation bins for  
 191      more accurate estimation of the surface mass balance of the big ice sheets. Ice accumu-  
 192      lation is modeled as a capping flux, or snow in excess of the assumed 10 m snow cap, and  
 193      refreezing of liquid within the snowpack additionally acts as a source of mass in the SMB  
 194      calculation. Since the 10 m snowcap needs to be reached in the accumulation zone to  
 195      simulate the SMB, the snow depths in the variable-resolution grids were spun-up by forc-  
 196      ing CLM5 standalone, cycling over 20 years of a fully coupled *ARCTIC* run for about  
 197      500 years. The uniform resolution grids are all initialized with an SMB from an exist-  
 198      ing f09 spun-up initial condition.

### 199      2.5 SMB Analysis

200      The SMB is the sum of the mass source term, accumulation (i.e., precipitation),  
 201      and the mass sink term, ablation. Ablation can be expressed as sublimation plus total  
 202      runoff, with runoff being a combination of liquid precipitation and snow and ice melt.  
 203      Not all liquid precipitation becomes runoff; rain may penetrate pore spaces in the firn  
 204      layer and freeze, forming ice lenses in the subsurface. All these processes are represented  
 205      by different components in CESM, but the surface mass balance proper is computed by  
 206      CLM. CLM uses a downscaling technique to account for sub-grid variability in SMB. In  
 207      short, the ice sheet patch in a CLM grid cell is subdivided into 10 elevation classes (EC),

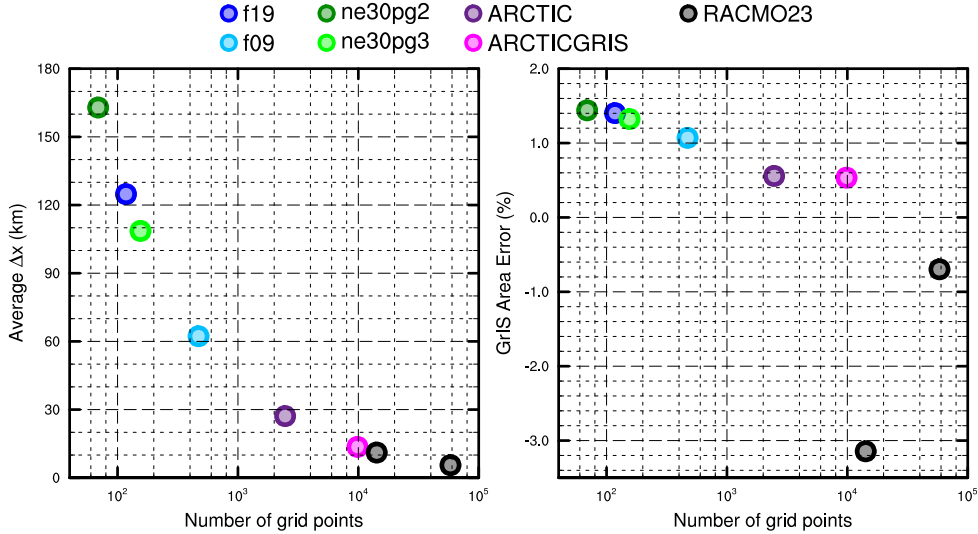


**Figure 3.** The spatial properties of the GrIS as represented by different grids in this study. (Left) approximate average grid spacing over GrIS, (right) GrIS area error, computed as the relative differences from a 4km dataset used to create the CESM ice masks.

weighted by their respective area fractions at each EC, which is derived from a high resolution GrIS elevation model. The near surface air temperature, humidity and air density are calculated at each EC using an assumed lapse rate and the elevation difference from the grid mean, allowing for the precipitation rates to be repartitioned into solid or liquid based on the temperature of each EC. This technique allows for a unique surface energy balance and surface mass balance at each EC. Integrating over all ECs using the area weights then provides a more accurate SMB. For a more detailed description of how the surface mass balance is computed in the CESM, see (van Kampenhout et al., 2020b).

Simulated SMB are compared against several observational data products. RACMO2.3 11km and RACMO2.3p2 5.5km regional simulations forced by reanalysis at its domain boundaries, performs very skillfully relative to observations and is therefore considered an ideal modeling target (Noël et al., 2019). The Land Ice Verification and Validation toolkit (LIVVkit), version 2.1 (Evans et al., 2019) maintains a repository of snow pit and ice core SMB measurements, as well as the IceBridge radar accumulation dataset.

A common high resolution dataset is used to generate the GrIS boundary conditions using the CLM dataset creation tools. Since we are interested in the total ice sheet SMB, we seek to integrate various components of the SMB over a common ice mask to get the total mass change over the GrIS. Figure 3 shows the GrIS ice mask area across the different grids, as a function of the number of grid points. Due to the use conservative regridding in the CLM tools, the interpolation errors are small and ice mask areas have less than 1.5% errors relative to the raw ice mask dataset. RACMO, however, uses a smaller ice mask, about 3% smaller than the raw CLM dataset. While Figure 3 suggests integrating quantities over the native ice mask of the six grids would probably not suffer from large errors due to differing ice masks, we seek to compare these integrated quantities with RACMO. Therefore, we have taken the approach of mapping all model fields to the lowest resolution grids and integrating over the respective low resolution ice masks. Due to the sensitivity of mapping errors to grid coordinates (i.e., unstructured or structured), all quantities are evaluated on both the *f19* and *ne30pg2* low resolution grids. In addition, two remapping packages are used; ESMF conservative and a TempestRemap

237 high-order, monotone algorithm. In all, each integrated quantity is evaluated (at most)  
 238 four times to provide an estimate of uncertainty due to differences in grid coordinates  
 239 and remapping algorithm.

## 240 3 Results

### 241 3.1 Tropospheric temperatures

242 Before delving into the simulated characteristics of the Arctic, the global mean dif-  
 243 ferences between the various grids and dycores are assessed. Figure 4 shows the clima-  
 244 tological, zonal mean height plots expressed as differences between the uniform resolu-  
 245 tion grids and dycores. The *f09* grid is warmer than the *f19* grid, primarily in the mid-  
 246 to-high latitudes and throughout the depth of the troposphere. This is a common response  
 247 to increasing horizontal resolution in GCMs (Pope & Stratton, 2002; Roeckner et al., 2006),  
 248 and (A. R. Herrington & Reed, 2020) has shown that this occurs in CAM due to greater  
 249 resolved vertical velocities that in turn, facilitate greater condensational heating in the  
 250 macrophysics routine in CLUBB. The right columns in Figure 4 supports this interpre-  
 251 tation, which shows an increase in the climatological CLUBB heating in the mid-latitudes  
 252 in the *f09* grid.

253 As the SE dycore is less diffusive than the FV dycore, the resolved vertical veloc-  
 254 ities are larger in the SE dycore, and so a modest, resolution-like sensitivity occurs in  
 255 which *ne30pg3* is warmer than *f09* (Figure 4). The stratosphere has a different response,  
 256 in which *ne30pg3* is much cooler than *f09* in the mid-to-high latitudes. The differences  
 257 in temperature between *ne30pg3* and *ne30pg2* are small, with a slight warming near the  
 258 tropopause at high latitudes. This is consistent with the similar climates found between  
 259 these grids in (A. R. Herrington et al., 2019).

260 Comparing the variable-resolution grids to the uniform resolution grids is compli-  
 261 cated because we simultaneously increase the grid resolution and reduce the physics time-  
 262 step, both of which noticeably impact the solution (D. L. Williamson, 2008). An additional  
 263 *ne30pg3* simulations is run with the physics time-step used in the *ARCTIC* grid, referred  
 264 to as *ne30pg3\**. Figure 5 shows the change in climatological temperature in zonal-mean  
 265 height space between *ne30pg3\** and *ne30pg3*. A similar warming response to increasing  
 266 resolution occurs when the time-step is reduced, and the mechanism is similar in that  
 267 the shorter time-step facilitates greater condensational heating by CLUBB. Figure 5 shows  
 268 the difference in climatological temperature between the *ARCTIC* grid and the *ne30pg3\**  
 269 grid. The greater condensational heating and warmer temperatures are confined to the  
 270 regionally refined region when the impact of physics time-steps is removed from the anal-  
 271 ysis.

### 272 3.2 Greenland surface mass balance

273 The surface mass balance (SMB) of the Greenland Ice Sheet (GrIS) is simulated  
 274 in all grids and dycores in this study. As the accuracy of the computed SMB is sensi-  
 275 tive to grid resolution, Figure 3 shows the average grid spacing for all six grids in this  
 276 study. The *ne30pg2* grid has the coarsest representation with an average  $\Delta x = 160 \text{ km}$ ,  
 277 and the *ARCTICGRIS* grid has the highest resolution with an average  $\Delta x = 14.6 \text{ km}$ ,  
 278 similar to the grid spacing of the  $11 \text{ km}$  RACMO model. The *ne30pg3* grid has an av-  
 279 erage  $\Delta x = 111.2 \text{ km}$ , which is substantially more coarse than the *f09* grid, having an  
 280 average  $\Delta x = 60 \text{ km}$ . This is interesting because *ne30pg3* and *f09* have similar aver-  
 281 age grid spacing over the entire globe, and comparable computational costs, but due to  
 282 the convergence of meridians the finite-volume model has enhanced resolution over GrIS.  
 283 The *ARCTIC* grid has an average grid spacing over GrIS of  $\Delta x = 27.8 \text{ km}$ , and is about  
 284 10 times more expensive than the  $1^\circ$  models. The *ARCTICGRIS* grid is about twice  
 285 as expensive as the *ARCTIC* grid.

The climatological mean precipitation bias over GrIS is shown in Figure 3, defined as differences from the RACMO2.3p2 5.5km solution (Noël et al., 2019). What sticks out is that the uniform  $1^{\circ} - 2^{\circ}$  grids have positive bias centered over the southern dome. The *ARCTIC* runs improves this bias substantially, and is all but eliminated in *ARCTCIGRIS* run. The southern dome bias is therefore due to inadequate horizontal resolution, which is consistent with the results of (van Kampenhout et al., 2018). Southeast Greenland has the largest accumulation rates in GrIS due to synoptic systems moving in from the southeast, which become orographically lifted by the steep southeast ice sheet margin, dumping large amounts of precipitation along the southeast coast. At lower horizontal resolutions, the topography is too smooth and large amounts of moisture penetrates further inland, incorrectly dumping large amounts of precipitation onto the interior of the ice sheet.

Figure 7 shows time-series of integrated precipitation and snow/ice melt over the GrIS in the various different grids and dycores, with both RACMO2.3 and 2.3p2 show in black. The 1979-1998 climatological mean values are provided as circles on the right side of the panels. The uniform  $1^{\circ}-2^{\circ}$  grids all show a distinctive positive bias in precipitation due to this over-prediction of interior precipitation rates. The variable-resolution grids have the smallest precipitation biases, providing a comparable solution to RACMO. The *f19* and *f09* perform similarly, with +110 Gt/yr bias, whereas *ne30pg3* is biased by about +170 Gt/yr and *ne30pg2*, +230 Gt/yr. The results suggest that uniform resolution spectral-element grids have larger biases than the finite-volume grids, consistent with spectral-element grids having a coarser representation of GrIS (Figure 3). While it seems likely that *ne30pg2* has the largest bias of all the grids, it's difficult to say for certain that the *ne30pg3* precipitation biases are worse than the finite-volume grids, owing to the use of a single realization for each grid.

The combined snow/ice melt integrated over the GrIS is given by the bottom panel of Figure 7. The *ARCTIC* grid simulates the most realistic melt rates, with all other grids tending to have larger melt rates than RACMO. The *ARCTCIGRIS* grid over predicts melting by about 150 Gt/yr. This is likely due to an anomalously warm lower troposphere during the summer, relative to the *ARCTIC* run (not shown). The *f19* and *f09* melting rates are improved over *ARCTCIGRIS*, with a positive melt bias between 70-90 Gt/yr. The spectral-element grids have the largest positive melt bias, between 210-230 Gt/yr.

Figure 8 shows the distribution of point-wise differences from LIVVkit observational database, as a violin plot. The IceBridge dataset is exclusively from the interior of the ice sheet and represents accumulation rates. The uniform  $1^{\circ}-2^{\circ}$  grids have similar median errors of about +35-50 mm.w.e, while the variable-resolution errors are noticeably smaller. The in-situ observations in the accumulation zone, shown in the middle plot looks very similar to the IceBridge errors, and so provides confidence that the variable-resolution grids are outperforming the uniform grids in the interior accumulation zone. The errors evaluated at in-situ ablation zone measurements are in tension with the RACMO results in Figure 7, indicating that the uniform  $1^{\circ}-2^{\circ}$  grids perform similarly, the *ARCTIC* grid showing a reduction in bias and the *ARCTCIGRIS* having the smallest bias of all the grids. However, the in-situ ablation measurements are sparse in time and space, and so there is a large uncertainty in extending these results to the entirety of the ablation zone.

The infamous k-transect mass balance profile is contained in the LIVVkit database, and shown in Figure 9, along with the all the simulations. The in-situ observation points seem to be nicely replicated by the *ARCTCIGRIS* run, whereas the *ARCTIC* grid seems to be biased positive in the higher-elevations of the ablation zone. The *f09* grid is surprisingly competitive with the variable-resolution grids, capturing a realistic slope of the elevation-SMB curve. The elevation-SMB slopes of the uniform spectral-element and *f19* grid simulate too shallow a slope in the higher elevation regions of the k-transect. Figure ?? shows

339 the representation of the surface of the ice sheet along these transects in the simulations,  
 340 compared to a high resolution elevation dataset. The  $1^{\circ}$ – $2^{\circ}$  grids are noticeably coarse,  
 341 with only a handful of grid cells populating the transect. The *f09* grid is a bit of an ex-  
 342 ception, since the grid cells become very narrow in the meridional direction at high lat-  
 343 itudes, and so a larger number of grid cells can populate the transect, consistent with  
 344 its skillful representation of the ablation zone.

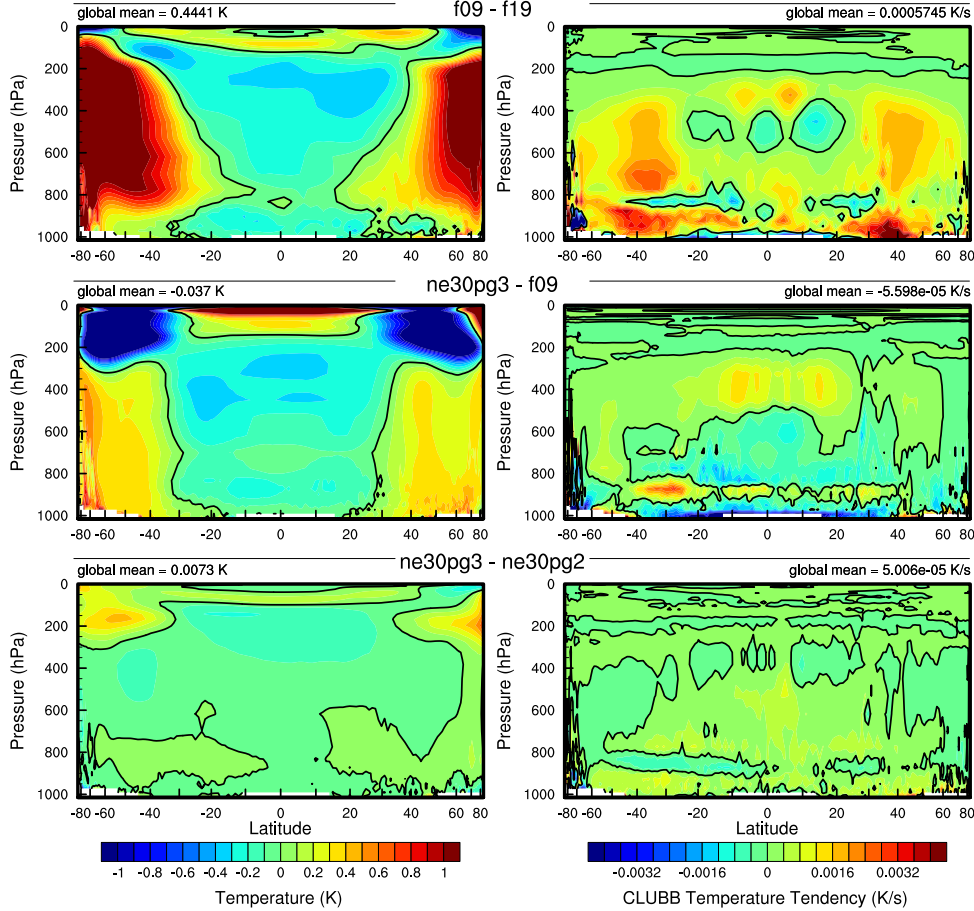
345 What the authors refer to as the “b-transect” in northwest Greenland (Figure 9)  
 346 is characterized by orographic precipitation, resulting in the accumulation zone extend-  
 347 ing down to the ice margin. The variable resolution grids perform relatively well, with  
 348 larger SMBs at lower elevations where the precipitation rates are highest, whereas the  
 349  $1^{\circ}$  –  $2^{\circ}$  grids underestimate the SMB in these lower elevation regions. Only the vari-  
 350 able resolution grids can capture the local reduction in SMB in the 1500-2000 m region.  
 351 The skill of the variable-resolution grids is clearly related to the accurate representation  
 352 of this steep transect, while also capturing the protrusion around 1500-2000 m that co-  
 353 incides with the local minimum in SMB (Figure ??).

### 354 3.3 Impact of horizontal resolution on extremes

355 Synoptic storms are identified and analyzed using TempestExtremes (Ullrich et al.,  
 356 2021). The new *ARCTIC* grid contains  $\frac{1}{4}^{\circ}$  refinement north of about  $45^{\circ}$  latitude, and  
 357 so the storm tracker is applied to this region for the *ARCTIC* and *ne30pg3* run to iden-  
 358 tify differences in storm characteristics due to horizontal resolution. Figure 11 shows the  
 359 mean precipitation rates averaged over all January storms identified by TempestExtremes.  
 360 The iconic comma structure of the mid-latitude cyclones is simulated in *ne30pg3* and  
 361 *ARCTIC* grids, with the magnitudes about the same in these two grids, with perhaps  
 362 a marginal increase in precipitation rates in the storm center of the *ARCTIC* grid. For  
 363 good measure, the *ne30pg3\** run is also plotted, and looks more-or-less identical to the  
 364 *ne30pg3* run.

365 As has been previously reported, horizontal resolution can have large impacts on  
 366 extreme precipitation events. Figure 12 is a PDF of the precipitation rates associated  
 367 with synoptic storms, by month. The *ARCTIC* run has larger extreme precipitation rates  
 368 compared to *ne30pg3* in every month, but the increase is greatest in the summer months,  
 369 which coincides with the most extreme events of the year. This is primarily due to an  
 370 increase in resolution; the *ne30pg3\** only marginally increases the precipitation rates com-  
 371 pared with *ne30pg3*. The *f09* and *f19* grids look similar to *ne30pg3*, but with *f09* hav-  
 372 ing more frequent extreme precipitation events than *f19* (not shown). It should also be  
 373 noted that the PDFs are evaluated on an identical composite grid for all runs, and so  
 374 storm statistics are not impacted by differences in output resolution.

375 The extreme precipitation rates in the *ARCTIC* run are closer to the ERA5 re-  
 376 analysis than in *ne30pg3* (Figure 12). It’s difficult to know the extent that the extreme  
 377 precipitation rates in ERA5 are constrained by data assimilation, or whether these pre-  
 378 cipitation rates are due to using a similar  $\frac{1}{4}^{\circ}$  model as the *ARCTIC* grid. However, pre-  
 379 cipitation rates in  $\frac{1}{4}^{\circ}$  models tend to produce more skillful extreme events (O’Brien et  
 380 al., 2016).

**Figure 4.**

### 381 3.4 Orographic gravity waves emanating from Greenland

### 382 3.5 Katabatic winds emanating from Greenland

## 383 4 Conclusions

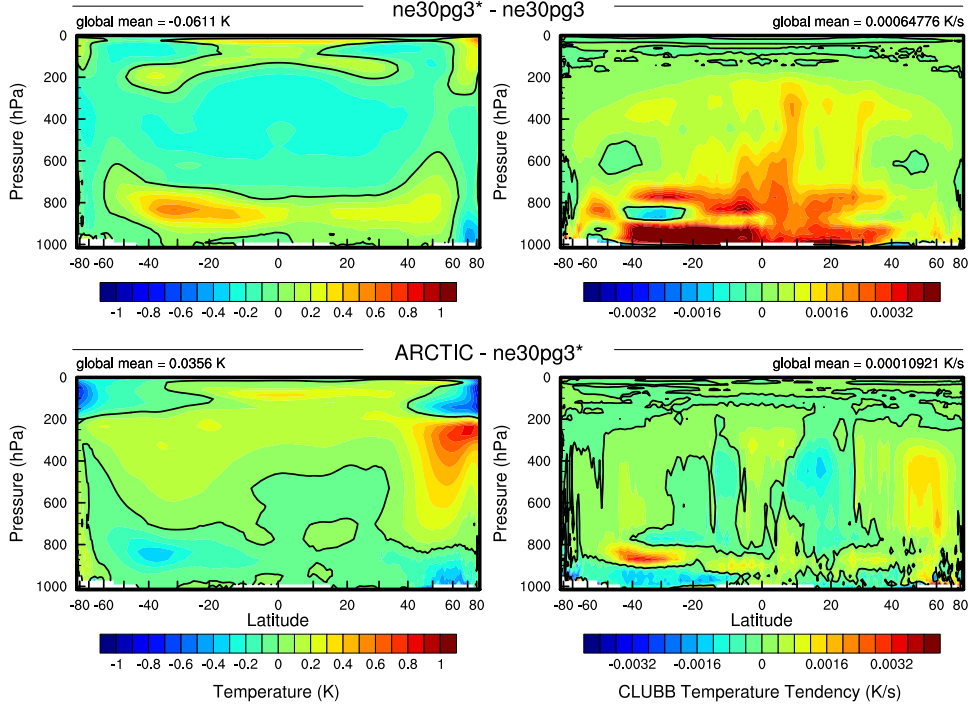
### 384 Acknowledgments

385 This material is based upon work supported by the National Center for Atmospheric Re-  
 386 search (NCAR), which is a major facility sponsored by the NSF under Cooperative Agree-  
 387 ment 1852977. Computing and data storage resources, including the Cheyenne super-  
 388 computer (doi:10.5065/D6RX99HX), were provided by the Computational and Infor-  
 389 mation Systems Laboratory (CISL) at NCAR.

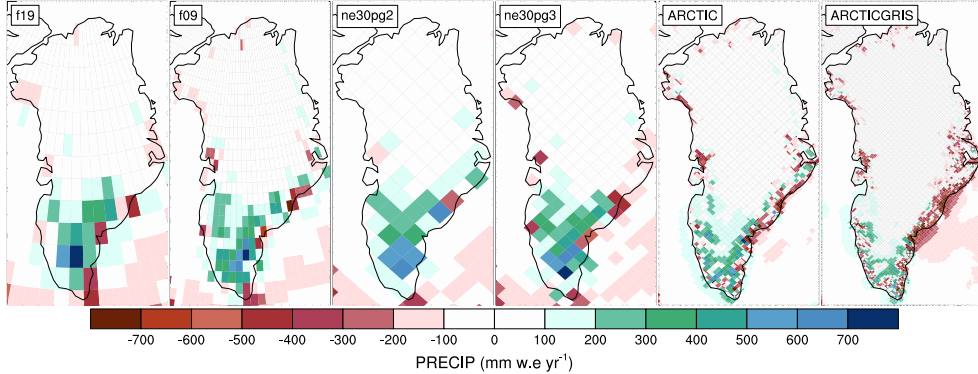
390 The data presented in this manuscript is available at <https://github.com/adamrher/2020-arcticgrids>.

## 392 References

- 393 Beljaars, A., Brown, A., & Wood, N. (2004). A new parametrization of turbulent  
 394 orographic form drag. *Quart. J. Roy. Meteor. Soc.*, 130(599), 1327–1347. doi:  
 395 10.1256/qj.03.73

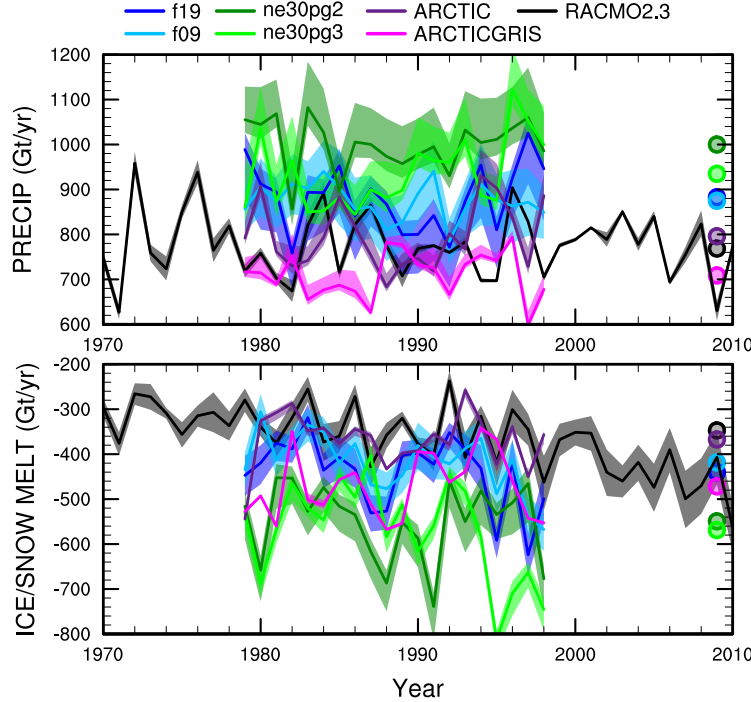
**Figure 5.**

- 396 Bogenschutz, P. A., Gettelman, A., Morrison, H., Larson, V. E., Craig, C., & Schaanen, D. P. (2013). Higher-order turbulence closure and its impact on climate  
397 simulations in the community atmosphere model. *Journal of Climate*, 26(23),  
398 9655–9676.
- 400 Bromwich, D. H., Cassano, J. J., Klein, T., Heinemann, G., Hines, K. M., Steffen,  
401 K., & Box, J. E. (2001). Mesoscale modeling of katabatic winds over greenland  
402 with the polar mm5. *Monthly Weather Review*, 129(9), 2290–2309.
- 403 Canuto, C., Hussaini, M. Y., Quarteroni, A., & Zang, T. (2007). *Spectral methods:  
404 Evolution to complex geometries and applications to fluid dynamics* (1st ed.).  
405 Springer.
- 406 Collins, W. D., Rasch, P. J., Boville, B. A., Hack, J. J., McCaa, J. R., Williamson,  
407 D. L., ... Zhang, M. (2006). The formulation and atmospheric simulation  
408 of the community atmosphere model version 3 (cam3). *Journal of Climate*,  
409 19(11), 2144–2161.
- 410 Dennis, J. M., Edwards, J., Evans, K. J., Guba, O., Lauritzen, P. H., Mirin, A. A.,  
411 ... Worley, P. H. (2012). CAM-SE: A scalable spectral element dynamical  
412 core for the Community Atmosphere Model. *Int. J. High. Perform. C.*, 26(1),  
413 74–89. Retrieved from <http://hpc.sagepub.com/content/26/1/74.abstract>  
414 doi: 10.1177/1094342011428142
- 415 Evans, K. J., Kennedy, J. H., Lu, D., Forrester, M. M., Price, S., Fyke, J., ... oth-  
416 ers (2019). Livykit 2.1: automated and extensible ice sheet model validation.  
417 *Geoscientific Model Development*, 12(3), 1067–1086.
- 418 Gettelman, A., Morrison, H., Santos, S., Bogsenschutz, P., & Caldwell, P. (2015).  
419 Advanced two-moment bulk microphysics for global models. part ii: Global  
420 model solutions and aerosol–cloud interactions. *Journal of Climate*, 28(3),  
421 1288–1307.
- 422 Golaz, J.-C., Larson, V. E., & Cotton, W. R. (2002). A pdf-based model for bound-



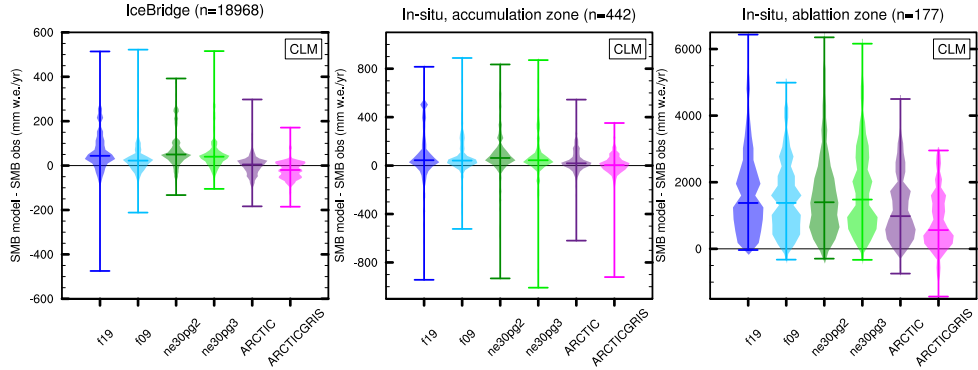
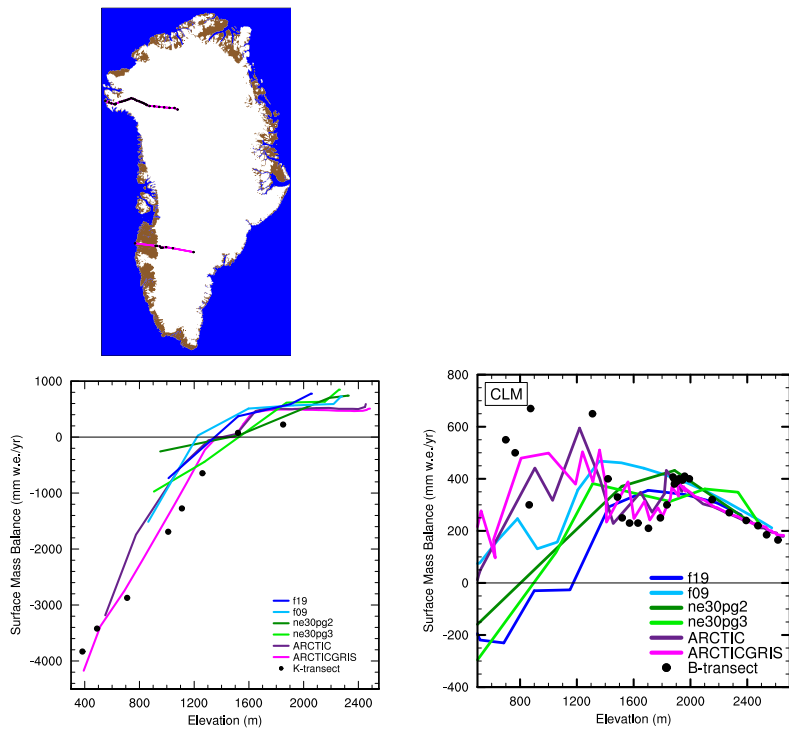
**Figure 6.** Climatological (1979–1998) annual precipitation rate bias (in mm/yr) relative to the RACMO2.3p2 5.5km resolution data product (Noël et al., 2019).

- 423      ary layer clouds. part i: Method and model description. *Journal of the Atmo-*  
 424      *spheric Sciences*, 59(24), 3540–3551. doi: 10.1175/1520-0469(2002)059<3540:
- 425      apbmfb>2.0.co;2
- 426      Guba, O., Taylor, M. A., Ullrich, P. A., Overfelt, J. R., & Levy, M. N. (2014). The  
 427      spectral element method (sem) on variable-resolution grids: evaluating grid  
 428      sensitivity and resolution-aware numerical viscosity. *Geosci. Model Dev.*, 7(6),  
 429      2803–2816. doi: 10.5194/gmd-7-2803-2014
- 430      Herrington, A., Lauritzen, P., Taylor, M. A., Goldhaber, S., Eaton, B. E., Bacmeis-  
 431      ter, J., ... Ullrich, P. (2018). Physics-dynamics coupling with element-based  
 432      high-order galerkin methods: quasi equal-area physics grid. *Mon. Wea. Rev.*,  
 433      47, 69–84. doi: 10.1175/MWR-D-18-0136.1
- 434      Herrington, A., & Reed, K. (2018). An idealized test of the response of the commu-  
 435      nity atmosphere model to near-grid-scale forcing across hydrostatic resolutions.  
 436      *J. Adv. Model. Earth Syst.*, 10(2), 560–575.
- 437      Herrington, A. R., Lauritzen, P. H., Reed, K. A., Goldhaber, S., & Eaton, B. E.  
 438      (2019). Exploring a lower resolution physics grid in cam-se-cslam. *Journal of*  
 439      *Advances in Modeling Earth Systems*, 11.
- 440      Herrington, A. R., & Reed, K. A. (2020). On resolution sensitivity in the commu-  
 441      nity atmosphere model. *Quarterly Journal of the Royal Meteorological Society*,  
 442      146(733), 3789–3807.
- 443      Hurrell, J. W., Hack, J. J., Shea, D., Caron, J. M., & Rosinski, J. (2008). A new  
 444      sea surface temperature and sea ice boundary dataset for the community at-  
 445      mosphere model. *Journal of Climate*, 21(19), 5145–5153.
- 446      Jablonowski, C., & Williamson, D. L. (2006). A baroclinic instability test case for  
 447      atmospheric model dynamical cores. *Q. J. R. Meteorol. Soc.*, 132, 2943–2975.
- 448      Jablonowski, C., & Williamson, D. L. (2011). The pros and cons of diffusion, fil-  
 449      ters and fixers in atmospheric general circulation models., in: P.H. Lauritzen,  
 450      R.D. Nair, C. Jablonowski, M. Taylor (Eds.), Numerical techniques for global  
 451      atmospheric models. *Lecture Notes in Computational Science and Engineering*,  
 452      Springer, 80.
- 453      Lauritzen, P. H., Bacmeister, J. T., Callaghan, P. F., & Taylor, M. A. (2015). Near  
 454      global model topography generation software for unstructured grids. *Geosci-  
 455      entific Model Development Discussions*, 8(6), 4623–4651. doi: 10.5194/gmdd-8  
 456      –4623–2015
- 457      Lauritzen, P. H., Mirin, A., Truesdale, J., Raeder, K., Anderson, J., Bacmeister, J.,  
 458      & Neale, R. B. (2011). Implementation of new diffusion/filtering operators  
 459      in the CAM-FV dynamical core. *Int. J. High Perform. Comput. Appl.*. doi:

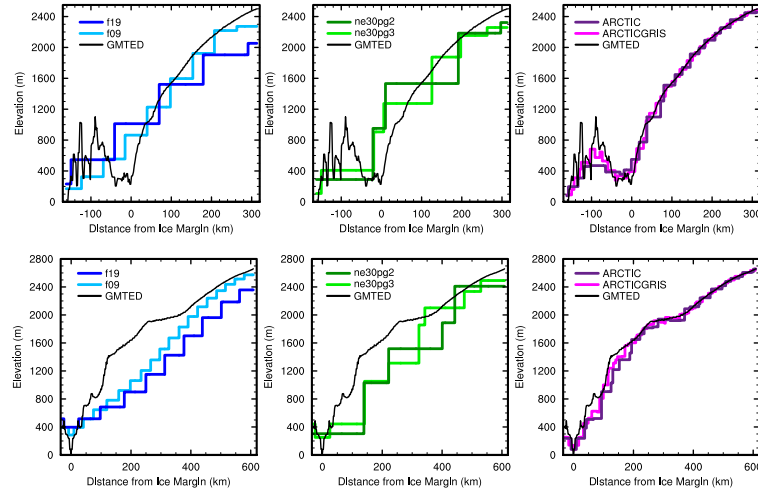
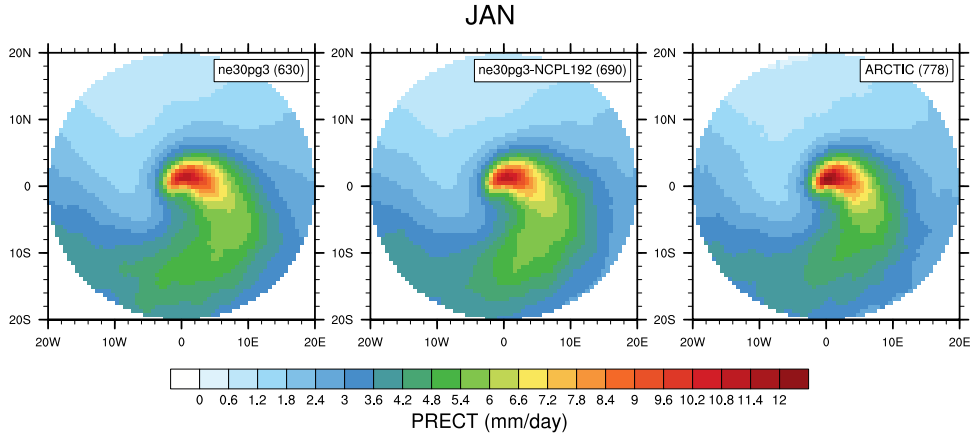


**Figure 7.** Time-series of annual (solid+liquid) precipitation (top) and annual runoff (bottom) integrated over the Greenland Ice Sheet for all six simulations and compared to RACMO3.2. The raw fields are mapped to two target low resolution grids, f19 & ne30pg2, and using two different remapping methods, conservative ESMF and high order TempestRemap. The remapped values are then integrated over the ice mask of the target grid. This gives four time-series for each simulation (three for f19 & ne30pg2), with the mean value given by the solid line and shading spanning the extent of the remapped solutions.

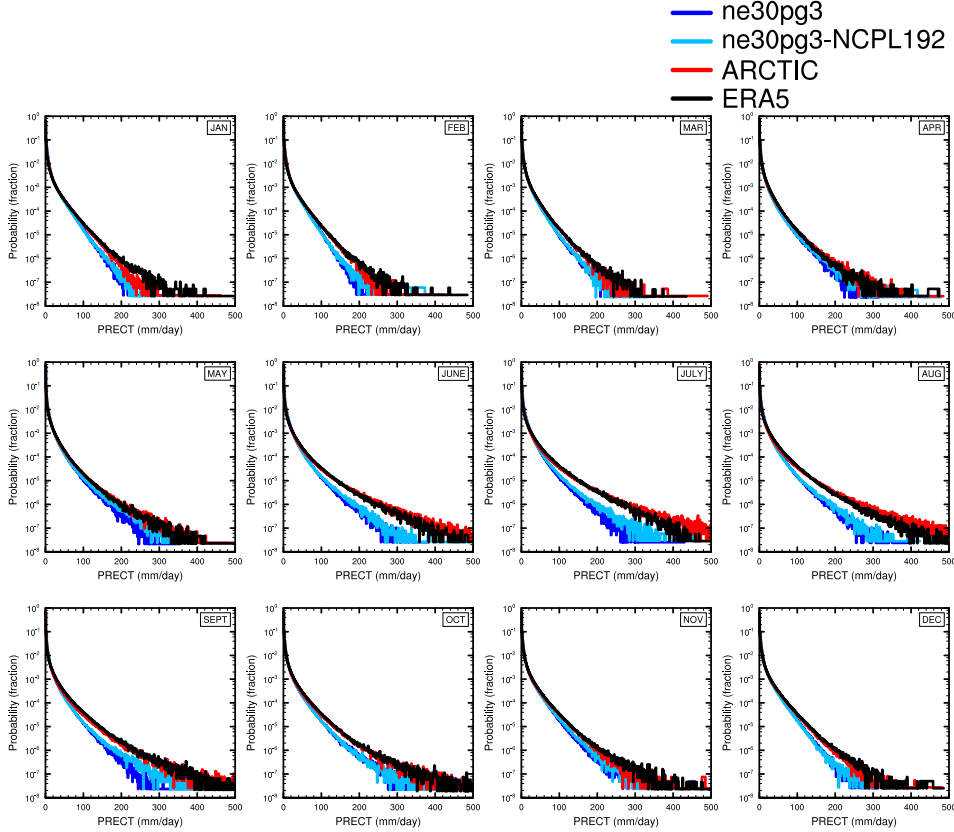
- 460 10.1177/1094342011410088  
 461 Lauritzen, P. H., Nair, R., Herrington, A., Callaghan, P., Goldhaber, S., Dennis, J.,  
 462 ... Dubos, T. (2018). NCAR CESM2.0 release of CAM-SE: A reformulation  
 463 of the spectral-element dynamical core in dry-mass vertical coordinates with  
 464 comprehensive treatment of condensates and energy. *J. Adv. Model. Earth  
 465 Syst.*. doi: 10.1029/2017MS001257  
 466 Lauritzen, P. H., Taylor, M. A., Overfelt, J., Ullrich, P. A., Nair, R. D., Goldhaber,  
 467 S., & Kelly, R. (2017). CAM-SE-CSLAM: Consistent coupling of a conser-  
 468 vative semi-lagrangian finite-volume method with spectral element dynamics.  
 469 *Mon. Wea. Rev.*, 145(3), 833-855. doi: 10.1175/MWR-D-16-0258.1  
 470 Lin, S.-J. (2004). A 'vertically Lagrangian' finite-volume dynamical core for global  
 471 models. *Mon. Wea. Rev.*, 132, 2293-2307.  
 472 Lin, S.-J., & Rood, R. B. (1997). An explicit flux-form semi-Lagrangian shallow-  
 473 water model on the sphere. *Q.J.R.Meteorol.Soc.*, 123, 2477-2498.  
 474 Lofverstrom, M., Fyke, J. G., Thayer-Calder, K., Muntjewerf, L., Vizcaino, M.,  
 475 Sacks, W. J., ... Bradley, S. L. (2020). An efficient ice sheet/earth sys-  
 476 tem model spin-up procedure for cesm2-cism2: Description, evaluation, and  
 477 broader applicability. *Journal of Advances in Modeling Earth Systems*, 12(8),  
 478 e2019MS001984.  
 479 Neale, R. B., Richter, J. H., & Jochum, M. (2008). The impact of convection on

**Figure 8.****Figure 9.**

- 480 ENSO: From a delayed oscillator to a series of events. *J. Climate*, 21, 5904-  
481 5924.  
482 Noël, B., van de Berg, W. J., Lhermitte, S., & van den Broeke, M. R. (2019). Rapid  
483 ablation zone expansion amplifies north greenland mass loss. *Science advances*,  
484 5(9), eaaw0123.  
485 O'Brien, T. A., Collins, W. D., Kashinath, K., Rübel, O., Byna, S., Gu, J., ...  
486 Ullrich, P. A. (2016). Resolution dependence of precipitation statistical  
487 fidelity in hindcast simulations. *J. Adv. Model. Earth Syst.*, 8(2), 976-  
488 990. Retrieved from <http://dx.doi.org/10.1002/2016ms000671> doi:  
489 10.1002/2016ms000671  
490 Pope, V., & Stratton, R. (2002). The processes governing horizontal resolution sensi-  
491 tivity in a climate model. *Climate Dynamics*, 19(3-4), 211–236.  
492

**Figure 10.****Figure 11.**

- 492 Putman, W. M., & Lin, S.-J. (2007). Finite-volume transport on various cubed-  
493 sphere grids. *J. Comput. Phys.*, 227(1), 55–78.
- 494 Richter, J. H., Sassi, F., & Garcia, R. R. (2010). Toward a physically based gravity  
495 wave source parameterization in a general circulation model. *J. Atmos. Sci.*,  
496 67, 136–156. doi: dx.doi.org/10.1175/2009JAS3112.1
- 497 Roeckner, E., Brokopf, R., Esch, M., Giorgetta, M., Hagemann, S., Kornblueh, L.,  
498 ... Schulzweida, U. (2006). Sensitivity of simulated climate to horizontal  
499 and vertical resolution in the echam5 atmosphere model. *Journal of Climate*,  
500 19(16), 3771–3791.
- 501 Smirnova, J., & Golubkin, P. (2017). Comparing polar lows in atmospheric reanal-  
502 yses: Arctic system reanalysis versus era-interim. *Monthly Weather Review*,  
503 145(6), 2375–2383.
- 504 Stocker, T. (2014). *Climate change 2013: the physical science basis: Working group*  
505 *i contribution to the fifth assessment report of the intergovernmental panel on*  
506 *climate change*. Cambridge university press.
- 507 Suarez, M. J., & Takacs, L. L. (1995). Volume 5 documentation of the aries/geos dy-  
508 namical core: Version 2.

**Figure 12.** .

- 509 Taylor, M. A., Tribbia, J., & Iskandarani, M. (1997). The spectral element method  
 510 for the shallow water equations on the sphere. *J. Comput. Phys.*, *130*, 92-108.  
 511 Ullrich, P. A., Zarzycki, C. M., McClenney, E. E., Pinheiro, M. C., Stansfield, A. M.,  
 512 & Reed, K. A. (2021). Tempestextremes v2. 1: a community framework for  
 513 feature detection, tracking and analysis in large datasets. *Geoscientific Model  
 Development Discussions*, 1–37.  
 514 van Kampenhout, L., Lenaerts, J. T., Lipscomb, W. H., Lhermitte, S., Noël, B.,  
 515 Vizcaíno, M., ... van den Broeke, M. R. (2020a). Present-day greenland  
 516 ice sheet climate and surface mass balance in cesm2. *Journal of Geophysical  
 517 Research: Earth Surface*, *125*(2), e2019JF005318.  
 518 van Kampenhout, L., Lenaerts, J. T., Lipscomb, W. H., Lhermitte, S., Noël, B.,  
 519 Vizcaíno, M., ... van den Broeke, M. R. (2020b). Present-day greenland  
 520 ice sheet climate and surface mass balance in cesm2. *Journal of Geophysical  
 521 Research: Earth Surface*, *125*(2).  
 522 van Kampenhout, L., Rhoades, A. M., Herrington, A. R., Zarzycki, C. M., Lenaerts,  
 523 J. T. M., Sacks, W. J., & van den Broeke, M. R. (2018). Regional grid refine-  
 524 ment in an earth system model: Impacts on the simulated greenland surface  
 525 mass balance. *The Cryosphere Discuss.*. doi: 10.5194/tc-2018-257  
 526 Williamson, D. (2007). The evolution of dynamical cores for global atmospheric  
 527 models. *J. Meteor. Soc. Japan*, *85*, 241-269.  
 528 Williamson, D. L. (2008). Convergence of aqua-planet simulations with increas-  
 529 ing resolution in the community atmospheric model, version 3. *Tellus A*, *60*(5),  
 530 848–862. doi: 10.1111/j.1600-0870.2008.00339.x  
 531

- 532 Zhang, G., & McFarlane, N. (1995). Sensitivity of climate simulations to the pa-  
533 rameterization of cumulus convection in the canadian climate centre general  
534 circulation model. *Atmosphere-ocean*, 33(3), 407-446.